
FAST: Foreground-aware Diffusion with Accelerated Sampling Trajectory for Segmentation-oriented Anomaly Synthesis

Xichen Xu¹ Yanshu Wang¹ Jinbao Wang² Xiaoning Lei³
 Guoyang Xie^{3*} Guannan Jiang^{3*} Zhichao Lu⁴

¹Global Institute of Future Technology, Shanghai Jiao Tong University, Shanghai, China

²School of Artificial Intelligence, Shenzhen University, Shenzhen, China

³Department of Intelligent Manufacturing, CATL, Ningde, China

⁴Department of Computer Science, City University of Hong Kong, Hong Kong, China

neptune_2333@sjtu.edu.cn isaac_wang@sjtu.edu.cn wangjb@szu.edu.cn
 leixn01, jianggn@catl.com guoyang.xie@ieee.org zhichao.lu@cityu.edu.hk[†]

Abstract

Industrial anomaly segmentation relies heavily on pixel-level annotations, yet real-world anomalies are often scarce, diverse, and costly to label. Segmentation-oriented industrial anomaly synthesis (SIAS) has emerged as a promising alternative; however, existing methods struggle to balance sampling efficiency and generation quality. Moreover, most approaches treat all spatial regions uniformly, overlooking the distinct statistical differences between anomaly and background areas. This uniform treatment hinders the synthesis of controllable, structure-specific anomalies tailored for segmentation tasks. In this paper, we propose **FAST**, a foreground-aware diffusion framework featuring two novel modules: the *Anomaly-Informed Accelerated Sampling* (AIAS) and the *Foreground-Aware Reconstruction Module* (FARM). AIAS is a training-free sampling algorithm specifically designed for segmentation-oriented industrial anomaly synthesis, which accelerates the reverse process through coarse-to-fine aggregation and enables the synthesis of state-of-the-art segmentation-oriented anomalies in as few as 10 steps. Meanwhile, FARM adaptively adjusts the anomaly-aware noise within the masked foreground regions at each sampling step, preserving localized anomaly signals throughout the denoising trajectory. Extensive experiments on multiple industrial benchmarks demonstrate that FAST consistently outperforms existing anomaly synthesis methods in downstream segmentation tasks. We release the code in <https://anonymous.4open.science/r/NeurIPS-938>.

1 Introduction

Motivation. Industrial anomaly segmentation plays a vital role in modern manufacturing, aiming to localize abnormal regions at the pixel level. Unlike traditional anomaly detection, which typically performs binary classification at the image or region level, anomaly segmentation requires more fine-grained and precise localization of abnormal patterns. However, real-world anomalies are inherently scarce, diverse, and non-repeatable, making it difficult to collect data that fully captures the range of possible abnormal types. Moreover, acquiring high-quality pixel-level annotations is labor-intensive and costly, especially in industrial scenarios. To address these limitations, recent studies have increasingly explored the use of synthetic anomalies to expand the training data space and improve downstream performance.

Limitations. Despite recent advances, current anomaly synthesis methods face three fundamental limitations that hinder their effectiveness for segmentation tasks [31]. **(i) Lack of controllability.**

*Corresponding author.

[†]This work was supported by the National Natural Science Foundation of China (Grant No. 62206122) and the Tencent “Rhinoceros Birds” — Scientific Research Foundation for Young Teachers of Shenzhen University.

Most existing methods provide limited control over the structure, location, or extent of synthesized anomalies. This limitation is particularly evident in GAN-based approaches [20, 37, 5]. These methods typically adopt a one-shot generation paradigm, offering little flexibility in specifying where and how anomalies should appear. **(ii) Neglect of segmentation-relevant properties.** Training-free methods such as patch replacement or texture corruption [14, 36] may produce visible anomalies, but the synthesized patterns often lack the structural consistency and complexity of real-world industrial anomalies, which are critical for improving segmentation performance. **(iii) Uniform treatment of spatial regions and inefficiency.** Although recent diffusion-based methods [9, 12, 24] have mitigated the above issues, they still treat all spatial regions uniformly during both forward and reverse processes, without explicitly modeling the distinct statistical properties of anomaly regions [38, 34]. This absence of region-aware modeling prevents the model from preserving abnormal regions throughout the synthesis trajectory. Moreover, these models typically require hundreds to thousands of denoising steps [10, 25], resulting in a significant computational cost. While recent training-free methods [15] aim to accelerate sampling, they fail to incorporate anomaly-aware cues, making them less effective for segmentation-oriented industrial anomaly synthesis (SIAS). These limitations motivate the need for SIAS models that support **controllable anomaly synthesis, explicit modeling of anomaly regions, and efficient, task-aligned sampling strategies.**

FAST. To address these issues, we propose **FAST**, a novel foreground-aware diffusion framework with two complementary modules: **Anomaly-Informed Accelerated Sampling (AIAS)** and the **Foreground-Aware Reconstruction Module (FARM)**. (i) AIAS is a training-free sampling strategy that reduces the number of denoising steps by up to 99% (from 1000 to as few as 10), resulting in over 100× speedup for SIAS tasks. Despite this drastic acceleration, FAST achieves an average mIoU of 76.72% and accuracy of 83.97% on MVTec-AD, outperforming all prior state-of-the-art methods. (ii) FARM explicitly models abnormal regions by reconstructing pseudo-clean anomalies and generating anomaly-aware noise at each step in both the forward and reverse processes. Incorporating FARM boosts performance from 65.33% to 76.72% in mIoU (↑11.39), and from 71.24% to 83.97% in accuracy (↑12.73), demonstrating its critical role in enhancing anomaly salience. Detailed results are provided in Sec. 4.3. Together, AIAS and FARM enable FAST to generate controllable and segmentation-aligned anomalies that significantly improve downstream performance.

Contributions. In summary, our contributions are three-fold: (1) To mitigate the inefficiency and semantic misalignment of existing diffusion sampling, we introduce a training-free *Anomaly-Informed Accelerated Sampling* (AIAS) strategy that aggregates multiple denoising steps into a small number of coarse-to-fine analytical updates. (2) To address the lack of persistent anomaly-region representation, we propose a *Foreground-Aware Reconstruction Module* (FARM) that reconstructs pseudo-clean anomalies and reintegrates anomaly-aware noise at each step. (3) To support segmentation-oriented industrial anomaly synthesis, we design **FAST**, a controllable and efficient model. Extensive experiments on MVTec-AD and BTAD datasets demonstrate that it significantly outperforms existing methods in downstream segmentation tasks.

2 Related work

Industrial Anomaly Synthesis. Industrial anomaly synthesis aims to mitigate the scarcity of labeled abnormal samples in real-world inspection scenarios. Existing methods can be categorized into hand-crafted and DL-based approaches. Hand-crafted methods typically apply training-free manipulations to normal images, such as patch pasting [21, 23] or external texture blending [36, 32, 39] from sources like DTD [3], but they suffer from distributional deviation and limited realism. Deep learning-based methods alleviate these limitations by learning from real anomaly patterns. GAN-based methods [6, 28] can synthesize visually realistic anomalies but lack fine-grained controllability over anomaly shape and location. Diffusion-based methods [6, 13, 33] offer stronger generative capacity via large-scale pretrained models, yet treat all regions uniformly and lack explicit control over anomaly localization, which is essential for segmentation. To this end, we propose **FAST**, which integrates foreground-aware reconstruction and efficient, segmentation-oriented anomaly synthesis into a unified diffusion framework.

Acceleration of Discrete-Time Diffusion Models. Diffusion models can be categorized into continuous-time and discrete-time frameworks. Continuous formulations [16, 17, 41] adopt SDE/ODE-based parameterizations and leverage high-order solvers for efficient sampling. In contrast, standard DDPMs [10] model a discrete-time Markov chain with fixed variance schedules and require thousands of iterative denoising steps. While continuous-time solvers achieve notable speedups, they rely on continuously parameterized noise or score functions, which requires reformulating training

objectives or interface in discrete-time models. Therefore, various acceleration techniques have been developed specifically for discrete-time diffusion. Some methods modify the generative process to reduce steps: DDGAN [29] integrates GAN-based decoding, TLDM [40] and ES-DDPM [18] truncate the forward process, and Blurring Diffusion Models [11] operate in the frequency domain. However, these methods require retraining and show limited generalization. In contrast, training-free approaches such as DDIM [25], PLMS [15], and GGDM [27] accelerate sampling without model modification. Yet, they treat all spatial regions uniformly and lack task-specific guidance essential for SIAS. Recent work like CUT [26] introduces external prompts for localized control for anomalies, but at the cost of multiple iterations per sampling step. In comparison, **FAST** proposes a novel training-free strategy that aggregates multiple denoising steps into coarse-to-fine segments while injecting mask-aware structural guidance, enabling efficient SIAS.

3 Methods

FAST for Anomaly Segmentation. The proposed **FAST** framework is built upon the Latent Diffusion Model (LDM) [22] of T steps. For notational simplicity, we denote the encoded latent of the original image as x_0 , and its predicted reconstruction from the network as \hat{x}_0 . We define x_{t_s} as the noisy latent at timestep t_s , and \hat{x}_{t_s} as the FARM-adjusted, anomaly-aware latent at the same step. Let $\mathcal{M} \in \{0, 1\}^{H \times W}$ denote the binary anomaly mask, and $[t_s, t_e]$ represent a coarse-to-fine segment in AIAS, where $t_e < t_s$. Fig. 1 illustrates a single forward–reverse process at step t_s . In the forward phase, noise is added up to timestep t_s , yielding a noisy latent x_{t_s} . FARM (F_ϕ in Algorithm 1) then predicts a pseudo-clean anomaly latent \hat{x}_0^{an} , and adds noise to it up to timestep t_s to obtain an anomaly-aware latent \hat{x}_{t_s} , which aims to match the observed x_{t_s} in masked regions during training. In the corresponding reverse process, we divide the full denoising process into S segments, each spanning $[t_s, t_e]$. Within each segment, AIAS approximates the posterior transition using: $q(x_{t_e} | x_{t_s}, \hat{x}_0)$. This formulation aggregates multiple DDPM steps into a single numerical update. FARM is also applied to refine x_{t_e} , ensuring the preservation of anomaly cues throughout the reverse process. More details can be seen in Algorithms 1 and 2. In addition, for the textual conditioning component of LDM, we follow the configuration of Anomaly Diffusion [13]; more implementation details can be found there.

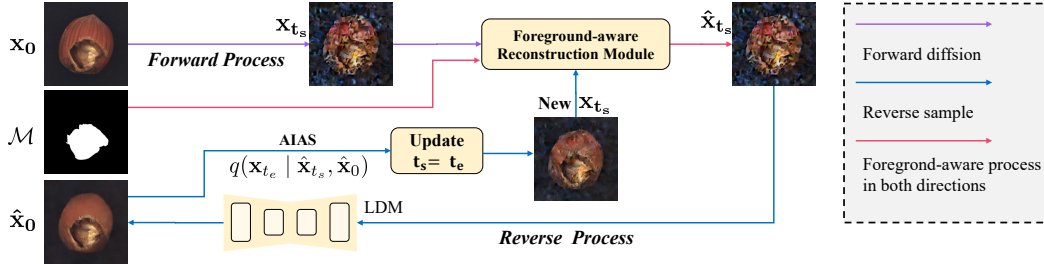


Figure 1: Illustration of a single forward–reverse process in FAST. **AIAS** accelerates sampling by aggregating multiple denoising steps into a small number of coarse-to-fine segments, achieving up to $100\times$ speedup while preserving semantic alignment under anomaly mask guidance. **FARM** extracts anomaly-only content from the noisy latent x_t at each timestep t and transforms it into anomaly-aware noise by re-applying forward diffusion.

Algorithm 1 FAST Training

- 1: **repeat**
- 2: $x_0 \sim q(x_0)$, \mathcal{M} , and weights λ_1, λ_2
- 3: $t_s \sim \text{Uniform}(\{1, \dots, T\})$, $\epsilon \sim \mathcal{N}(0, \mathbf{I})$
- 4: $x_{t_s} = \sqrt{\bar{\alpha}_{t_s}}x_0 + \sqrt{1 - \bar{\alpha}_{t_s}}\epsilon$
- 5: $\hat{x}_{t_s} = \sqrt{\bar{\alpha}_{t_s}}F_\phi(x_{t_s}, \mathcal{M}) + \sqrt{1 - \bar{\alpha}_{t_s}}\epsilon$
- 6: Take gradient descent step on:

$$\begin{aligned} & \nabla_\theta \|\epsilon - \epsilon_\theta(\hat{x}_{t_s}, t_s)\|^2 \\ & + \nabla_\phi \|\mathcal{M} \odot x_0 - F_\phi(x_{t_s}, t_s, \mathcal{M})\|^2 \end{aligned}$$

- 7: **until** converged

Algorithm 2 FAST Sampling

(Details are shown in Supplementary Material A.4)

- 1: Initialize $x_T \sim \mathcal{N}(0, \mathbf{I})$
- 2: **for** each segment $[t_s, t_e]$ from $T \rightarrow 0$ **do**
- 3: $\hat{\epsilon} = \epsilon_\theta(x_{t_s}, t_s)$
- 4: $\hat{x}_0 = \frac{1}{\sqrt{\bar{\alpha}_{t_s}}}(x_{t_s} - \sqrt{1 - \bar{\alpha}_{t_s}} \cdot \hat{\epsilon})$
- 5: **AIAS:**

$$x_{t_e} = F_\phi(q(x_{t_e} | x_{t_s}, \hat{x}_0), t_e, \mathcal{M})$$

- 6: **end for**
- 7: **return** x_0

3.1 Anomaly-Informed Accelerated Sampling

Standard DDPM allows us to directly compute the marginal distribution of x_t given a clean sample x_0 and additive noise ϵ . Therefore, the one-step posterior distribution of x_{t-1} can be expressed as:

$$q(x_{t-1} | x_t, x_0) = \mathcal{N}(A_t x_0 + B_t x_t, \sigma_t^2 \mathbf{I}), \quad (1)$$

where the coefficients are derived from the variance schedule as follows:

$$A_t = \frac{\sqrt{\bar{\alpha}_{t-1}} \beta_t}{1 - \bar{\alpha}_t}, \quad B_t = \frac{\sqrt{\alpha_t} (1 - \bar{\alpha}_{t-1})}{1 - \bar{\alpha}_t}, \quad \sigma_t^2 = \frac{1 - \bar{\alpha}_{t-1}}{1 - \bar{\alpha}_t} \beta_t,$$

and $\alpha_t = 1 - \beta_t$, $\bar{\alpha}_t = \prod_{s=1}^t \alpha_s$. All are closed-form coefficients derived from a predefined noise schedule. In practice, the true sample x_0 is not accessible during inference, and is typically replaced by a model prediction \hat{x}_0 obtained via denoising estimation. **Equation 1 thus serves as the foundation for approximate posterior sampling, provided that \hat{x}_0 is a sufficiently accurate estimate of the ground truth x_0 .**

Theoretically, if we assume $\hat{x}_0 = x_0$ holds exactly (i.e., the prediction perfectly matches the ground-truth image), then the entire reverse process becomes fully deterministic and analytically tractable, with the only source of stochasticity being the injected noise at each step. In this idealized setting, the reverse sampling trajectory is fully governed by closed-form probabilistic transitions. This forms the basis for Lemma 1 (For brevity, the full proof is provided in the Supplementary Material A.1).

Lemma 1 (Linear-Gaussian closure). Let $\{x_k\}_{k=0}^K \subset \mathbb{R}^d$ satisfy the recursion

$$x_{k-1} = C_k x_k + d_k + \epsilon_k, \quad \epsilon_k \sim \mathcal{N}(0, \Sigma_k), \quad \epsilon_k \perp \{x_k, \epsilon_{k+1}, \dots\}, \quad (2)$$

where $C_k \in \mathbb{R}^{d \times d}$, $d_k \in \mathbb{R}^d$, and $\Sigma_k \in \mathbb{R}^{d \times d}$ are deterministic. Then, for every integer m with $1 \leq m \leq k$, x_{k-m} is again an affine-Gaussian function of x_k :

$$x_{k-m} = \underbrace{\left(\prod_{i=0}^{m-1} C_{k-i} \right)}_{=: C_k^{(m)}} x_k + \underbrace{\sum_{i=0}^{m-1} \left(\prod_{j=1}^i C_{k-j} \right) d_{k-i}}_{=: d_k^{(m)}} + \epsilon_k^{(m)}, \quad (3)$$

where $\epsilon_k^{(m)} \sim \mathcal{N}(0, \Sigma_k^{(m)})$, $\Sigma_k^{(m)} = \sum_{i=0}^{m-1} \left(\prod_{j=1}^i C_{k-j} \right) \Sigma_{k-i} \left(\prod_{j=1}^i C_{k-j} \right)^\top$. (4)

While the ideal condition $\hat{x}_0 = x_0$ rarely holds in practice, the following properties justify the use of \hat{x}_0 in the multi-step formulation:

- (i) The training objective of standard DDPM is explicitly designed to minimize the discrepancy between the predicted noise and the true noise. Consequently, the denoising model $\epsilon_\theta(x_t, t)$ implicitly learns to reconstruct a close approximation of x_0 through the reverse reparameterization formula.
- (ii) Both empirical observations and theoretical analyses suggest that \hat{x}_0 varies slowly with respect to t at large diffusion steps. That is, for a segment $[t_s, t_e]$ with $t_s > t_e$ and moderate length (e.g., $t_s - t_e \ll T$), we have $\hat{x}_0(x_{t_s}, t_s) \approx \hat{x}_0(x_t, t)$ for all $t \in [t_e, t_s]$, due to the temporal smoothness of model predictions in the noise-dominated regime.

Therefore, it is reasonable to treat \hat{x}_0 as fixed within a short temporal window. Under this assumption, multiple single-step reverse transitions can be analytically composed into a single multi-step affine-Gaussian kernel. This approximation and Lemma 1 form the basis for Theorem 2, which characterizes the closed-form reverse process from t_s to t_e (For brevity, the full proof is provided in the Supplementary Material A.2).

Lemma 2 (Closed-form reverse from $t_s \rightarrow t_e$). Fix indices $0 \leq t_e < t_s \leq T$, and let the single-step coefficients (A_t, B_t, σ_t^2) be defined as in Eq. 13. Then the aggregated reverse kernel over $t_s \rightarrow \dots \rightarrow t_e$ is affine-Gaussian:

$$x_{t_e} = \Pi_{t_e}^{t_s} x_{t_s} + \Sigma_{t_e}^{t_s} \hat{x}_0 + \epsilon_{t_e}, \quad (5)$$

where

$$\Pi_{t_e}^{t_s} := \prod_{i=t_e+1}^{t_s} B_i, \quad \Sigma_{t_e}^{t_s} := \sum_{i=t_e+1}^{t_s} A_i \prod_{j=i+1}^{t_s} B_j, \quad \epsilon_{t_e} \sim \mathcal{N}\left(0, \sum_{i=t_e+1}^{t_s} \left(\prod_{j=i+1}^{t_s} B_j \right)^2 \sigma_i^2 \mathbf{I}\right).$$

Therefore, it can be observed that in the limited segments (e.g., $t_s \rightarrow t_e$), there are the three scalars $(\Pi_{t_e}^{t_s}, \Sigma_{t_e}^{t_s}, \varepsilon_{t_e})$, allowing us to precompute them once and re-use them during sampling. **Lemma. 2 enables theoretical computation of posterior transitions between any two timesteps t_s and t_e , allowing multi-step sampling in a manner distinct from DDIM.** However, while the affine-Gaussian transition provides an efficient coarse approximation for the reverse path $x_{t_s} \rightarrow x_{t_e}$, the approximation may introduce residual artifacts in practice. It is caused by the strong noise attenuation and the fixed \hat{x}_0 assumption. Moreover, since x_t inherently entangles both the foreground and the background content, direct sampling through the affine-Gaussian kernel will ignore the critical spatial structure discrepancies for SIAS.

To better preserve anomaly-localized information while ensuring smooth global composition, we explicitly decompose the clean sample x_0 into two disjoint components:

$$\mathbf{x}_0 = \mathbf{x}_0^{\text{an}} + \mathbf{x}_0^{\text{bg}}, \quad (6)$$

where \mathbf{x}_0^{an} is the anomaly-only region (masked by \mathcal{M}), and \mathbf{x}_0^{bg} is the background. The background is independently forward-diffused:

$$\mathbf{x}_{t_e}^{\text{bg}} \sim q(\mathbf{x}_{t_e}^{\text{bg}} | \mathbf{x}_0^{\text{bg}}), \quad (7)$$

while the anomaly foreground is refined by the learned FARM module (introduced later in Sec. 3.2), and merged with the background through spatial masking:

$$\mathbf{x}_{t_e}^R = \text{FARM}(\mathbf{x}_{t_e}), \quad \mathbf{x}_{t_e} = \mathcal{M} \odot \mathbf{x}_{t_e}^R + (1 - \mathcal{M}) \odot \mathbf{x}_{t_e}^{\text{bg}}. \quad (8)$$

This foreground-aware fusion ensures consistent noise levels between anomalous and normal regions at each step, preserving local anomaly salience while maintaining global visual coherence. In practice, we also introduce a final fine-grained refinement stage using standard DDPM posterior sampling for small t (e.g., $t = 1$ or $t = 2$) to restore the alignment between the coarse trajectory and the ground-truth posterior, and to enhance fine-scale texture fidelity. The complete sampling algorithm is summarized in Algorithm 3.

3.2 Foreground-Aware Reconstruction Module

As discussed above, conventional diffusion models treat all spatial regions uniformly, which limits their ability to synthesize localized anomalies. To address this, we propose the *Foreground-Aware Reconstruction Module* (FARM), which reconstructs clean anomaly-only content from noisy latent inputs under both **temporal** and **spatial guidance**. As illustrated in Fig. 2, FARM adopts an encoder-decoder architecture. The encoder f_{enc} extracts deep representations from the noisy latent x_{t_s} , while the decoder f_{dec} progressively upsamples and integrates the binary mask \mathcal{M} at multiple resolutions, ensuring spatial alignment with anomaly regions throughout the hierarchy.

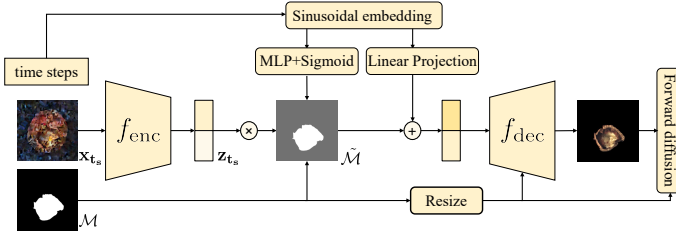


Figure 2: The architecture of FARM. Given noisy latent x_{t_s} and mask \mathcal{M} , the encoder f_{enc} extracts features z_{t_s} , which is also modulated by a background-adaptive soft mask $\tilde{\mathcal{M}}$ and related timestep embedding τ_{t_s} . The decoder f_{dec} then reconstructs the anomaly-only latent \hat{x}_0^{an} , which is forward-diffused to produce anomaly-aware noise.

To encode temporal context, we initialize sinusoidal timestep embeddings $\tau_{t_s} \in \mathbb{R}^d$ and project them into latent space via a learned linear layer. These embeddings are added to the encoder output, modulating feature responses based on the current noise level and allowing the decoder to reconstruct temporally consistent structures.

In addition, to modulate background activation, we introduce a background-adaptive soft mask:

$$\tilde{\mathcal{M}} = \mathcal{M}_d + (1 - \mathcal{M}_d) \cdot \sigma(f_{\text{bg}}(\tau_{t_s})), \quad (9)$$

where \mathcal{M}_d is a downsampled binary mask aligned with encoder resolution, and f_{bg} is a lightweight MLP. This design allows FARM to suppress irrelevant background features while adapting to the current timestep.

The encoded feature is computed as:

$$z_{t_s} = \tilde{\mathcal{M}} \cdot f_{\text{enc}}(\mathbf{x}_{t_s}) + \text{Proj}(\tau_{t_s}), \quad (10)$$

and decoded into an anomaly-only latent: $\hat{x}_0^{\text{an}} = f_{\text{dec}}(z_{t_s}, \mathcal{M})$.

To inject anomaly-aware noise into the sampling trajectory, the reconstructed anomaly is forward-diffused:

$$\hat{x}_{t_s}^{\text{an}} = \sqrt{\bar{\alpha}_{t_s}} \cdot \hat{x}_0^{\text{an}} + \sqrt{1 - \bar{\alpha}_{t_s}} \cdot \epsilon, \quad \epsilon \sim \mathcal{N}(0, \mathbf{I}), \quad (11)$$

and replaces the original noise in masked regions:

$$\hat{x}_{t_s} = (1 - \mathcal{M}) \cdot x_{t_s} + \mathcal{M} \cdot \hat{x}_{t_s}^{\text{an}}. \quad (12)$$

During training, FARM is supervised to ensure that the reconstructed anomalies match the masked regions of the noisy inputs. During inference, temporal and spatial guidance together enable FARM to introduce localized and temporally coherent anomaly signals into the reverse trajectory, ensuring alignment with the global generative process while enhancing fine-grained control.

4 Experiments

4.1 Implementation Details.

Datasets. We evaluate FAST on two widely-used industrial anomaly segmentation benchmarks: **MVTec-AD** [1] and **BTAD** [19]. For each anomaly class, we synthesize image-mask pairs using normal images, binary masks, and text prompts describing anomaly semantics. A total of 500 samples are generated per class, with approximately one-third used for training and the remainder reserved for evaluation. **Evaluation Metrics.** We report performance using **mean Intersection over Union (mIoU)** and **pixel-wise accuracy (Acc)**, following standard practice in anomaly segmentation. **Baselines.** FAST is compared against six representative anomaly synthesis approaches: CutPaste [14], DRAEM [36], GLASS [2], the GAN-based SOTA method DFMGAN [7], and diffusion-based SOTA models Anomaly Diffusion [13] and RealNet [38]. To simulate realistic deployment scenarios, we pair all generation methods with lightweight segmentation networks, including Segformer [30], BiSeNet V2 [35], and STDC [8]. As our method adopts the same prompt-driven synthesis setup as AnomalyDiffusion [13], we omit the details here for brevity. **Full specifications of the textual configuration, as well as other implementation details, including dataset preprocessing, sampling schedules, loss weights, and hyperparameter settings, are provided in the Supplementary Materials A.5.**

4.2 Comparison Studies

Table 1: Evaluation of pixel-level segmentation accuracy on extended MVTec data using real-time Segformer. **Detailed per-category results for other real-time segmentation model, such as BiSeNet V2 and STDC are reported in Supplementary Material A.6.**

Category	CutPaste		DRAEM		GLASS		DFMGAN		RealNet		AnomalyDiffusion		FAST	
	mIoU ↑	Acc ↑	mIoU ↑	Acc ↑	mIoU ↑	Acc ↑	mIoU ↑	Acc ↑	mIoU ↑	Acc ↑	mIoU ↑	Acc ↑	mIoU ↑	Acc ↑
bottle	75.11	79.49	79.51	84.99	70.26	76.30	75.45	80.39	77.96	83.90	76.39	83.54	86.86	90.90
cable	55.40	60.49	64.52	70.77	58.81	62.32	62.10	64.87	62.51	69.27	62.49	74.48	73.71	77.94
capsule	35.15	40.29	51.39	62.32	34.12	38.04	41.29	15.83	46.76	51.91	37.73	44.72	63.22	71.12
carpet	66.34	77.59	72.57	81.28	70.11	77.56	71.33	83.69	68.84	79.15	64.67	73.59	73.84	83.53
grid	29.90	46.72	47.75	67.85	37.43	46.30	37.73	54.13	37.55	48.86	38.70	51.82	52.45	70.70
hazel_nut	56.95	60.72	84.22	89.74	55.51	57.43	83.43	86.03	60.18	63.49	59.33	67.48	90.81	94.79
leather	57.23	63.49	64.12	71.49	62.05	73.38	60.96	68.02	68.29	77.16	56.45	62.51	66.60	74.18
metal_nut	88.78	90.94	93.51	96.10	88.15	90.52	92.77	94.93	91.28	94.09	88.00	91.10	94.65	96.88
pill	43.28	47.11	46.99	49.76	41.52	43.54	87.19	90.05	47.32	58.31	83.21	89.00	90.17	94.07
screw	25.10	31.35	46.96	59.03	35.94	42.37	46.65	50.79	47.12	55.17	38.47	49.49	49.94	57.48
tile	85.33	91.60	89.21	93.74	85.67	90.28	88.87	91.96	83.53	87.30	84.29	89.72	90.13	93.77
toothbrush	39.40	63.93	65.35	79.43	53.75	60.46	61.00	70.50	57.68	72.03	48.68	64.41	74.98	88.63
transistor	65.03	71.05	59.96	62.18	29.28	30.67	73.56	78.48	63.71	66.79	79.27	91.74	91.80	94.50
wood	49.64	60.47	67.52	73.28	50.91	53.16	67.00	80.84	61.84	89.54	60.16	74.62	78.77	86.31
zipper	65.39	71.89	69.29	79.36	69.98	79.31	66.34	70.50	68.78	78.50	65.36	72.66	72.80	84.73
Average	55.87	63.81	66.86	74.75	56.23	61.44	67.71	72.07	62.89	71.70	62.88	72.06	76.72	83.97

Table 2: Evaluation of pixel-level segmentation accuracy on extended BTAD data using real-time Segformer, BiSeNet V2 and STDC.

Backbone	Category	CutPaste		DRAEM		GLASS		DFMGAN		RealNet		AnomalyDiffusion		FAST	
		mIoU ↑	Acc ↑	mIoU ↑	Acc ↑	mIoU ↑	Acc ↑	mIoU ↑	Acc ↑	mIoU ↑	Acc ↑	mIoU ↑	Acc ↑	mIoU ↑	Acc ↑
Segformer	01	66.94	78.20	67.86	80.14	68.02	79.57	67.02	78.03	67.17	80.20	66.55	76.31	75.93	86.12
	02	65.04	83.64	69.52	82.96	69.99	83.58	68.75	84.92	70.64	83.90	68.06	84.74	70.63	81.63
	03	50.96	60.41	50.39	54.30	51.77	53.53	38.95	41.55	48.76	57.50	54.85	80.20	79.40	85.64
BiSeNet V2	01	57.15	69.88	49.16	63.48	44.09	50.57	49.49	59.20	45.45	57.65	46.66	55.18	58.74	68.98
	02	59.45	82.05	66.46	80.29	66.37	79.46	66.02	79.21	66.11	81.67	65.57	84.00	68.02	82.40
	03	31.84	40.62	36.15	39.04	30.80	37.15	20.12	21.48	29.55	33.11	42.27	74.41	77.87	92.49
STDC	01	48.06	59.86	42.17	65.36	45.51	60.12	44.68	51.71	32.91	49.21	44.85	55.29	44.95	53.47
	02	59.80	77.57	64.96	84.32	65.02	81.94	64.85	75.32	64.00	82.64	64.73	78.93	67.76	82.16
	03	19.76	25.20	36.14	38.80	17.04	28.01	14.67	16.55	22.57	24.79	41.71	65.45	84.04	92.36

Anomaly Segmentation Table. 1 and 2 report pixel-level segmentation results on various datasets using Segformer trained with FAST-augmented data. We observe that FAST achieves an average mIoU of 76.72% and accuracy of 83.97%, significantly outperforming the strongest prior method, DRAEM (74.75% Acc), by 9.22 points, respectively. Improvements are particularly notable in challenging categories: in *capsule*, FAST increases mIoU from 51.39% (DRAEM) to 63.22% (↑11.83); on *grid*, from 47.75% to 52.45% (↑4.70); and on *transistor*, from 84.22% to 91.80% (↑7.58). Even in

relatively easier categories such as *bottle* and *tile*, FAST still yields consistent improvements of 7.35 and 0.92 mIoU points, respectively. These results demonstrate that the combination of mask-aware noise injection via FARM and coarse-to-fine accelerated sampling via AIES enables more realistic and structurally coherent anomaly synthesis, leading to superior segmentation performance. Similar trends are observed when replacing Segformer with other real-time backbones such as BiseNetV2 and STDC, as shown in Supplementary Materials A.6, confirming the generalizability of FAST across different segmentation architectures.

Qualitative Comparison. Fig. 3

visually compares anomaly samples synthesized by different anomaly synthesis methods across several MVTEC-AD categories. It can be observed that traditional unsupervised methods such as CutPaste and DRAEM generate anomalies by overlaying arbitrary textures or patches without any semantic guidance. For instance, in the *Cable* category, anomalies produced by CutPaste appear as artificial, block-like overlays lacking meaningful texture or structure. Similarly, DRAEM and GLASS introduce unrealistic color distortions and incoherent patterns in the *Transistor* category, which deviate significantly from typical industrial anomalies. DL-based approaches (DFMGAN, RealNet, and AnomalyDiffusion) generate more visually plausible results, but still exhibit noticeable shortcomings. For instance, RealNet often introduces color shifts and boundary artifacts, as seen in the *tile* and *cable* cases, where anomalies appear overly smooth or blurred. DFMGAN and AnomalyDiffusion are able to synthesize more coherent shapes (e.g., spray-paint-like anomalies in *hazel_nut*), yet they suffer from inaccurate boundaries and structural mismatches, as is especially evident in the *tile* (AnomalyDiffusion) and *cable* (DFMGAN) categories. In contrast, FAST consistently produces anomalies that closely resemble realistic defects while maintaining precise alignment with the annotated masks. In the *metal_nut* and *hazel_nut* cases, FAST is the only method that preserves both texture and shape fidelity within the intended regions, demonstrating superior controllability and structural consistency. These results validate the effectiveness of the proposed FAST in segmentation-oriented anomaly synthesis.

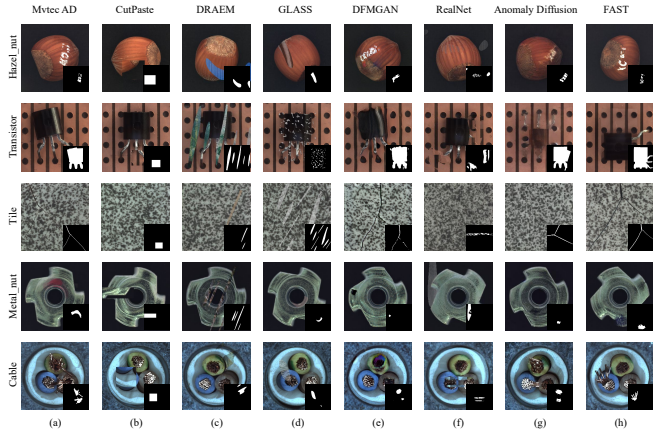


Figure 3: Visualization results of different anomaly synthesis methods on the MVTEC dataset. **Columns correspond to synthesis methods** (from left to right: MVTEC AD, CutPaste, DRAEM, GLASS, DFMGAN, RealNet, Anomaly Diffusion, FAST), and **rows correspond to product categories** (from top to bottom: hazel_nut, transistor, tile, metal_nut, cable).

For instance, RealNet often introduces color shifts and boundary artifacts, as seen in the *tile* and *cable* cases, where anomalies appear overly smooth or blurred. DFMGAN and AnomalyDiffusion are able to synthesize more coherent shapes (e.g., spray-paint-like anomalies in *hazel_nut*), yet they suffer from inaccurate boundaries and structural mismatches, as is especially evident in the *tile* (AnomalyDiffusion) and *cable* (DFMGAN) categories. In contrast, FAST consistently produces anomalies that closely resemble realistic defects while maintaining precise alignment with the annotated masks. In the *metal_nut* and *hazel_nut* cases, FAST is the only method that preserves both texture and shape fidelity within the intended regions, demonstrating superior controllability and structural consistency. These results validate the effectiveness of the proposed FAST in segmentation-oriented anomaly synthesis.

4.3 Ablation Studies

The Impact of AIAS.

We compare our proposed AIAS strategy with several widely-used training-free samplers, including DDPM [10] with 1000 steps, DDIM [25] with 50 steps and PLMS [15] with 50 steps. These methods represent state-of-the-art discrete-time sampling approaches for diffusion-based models. To ensure fairness, we exclude continuous-time solvers, as they rely on a fundamentally different formulation based on ODEs or SDEs, which necessitates a distinct training paradigm and architectural adjustments incompatible with our discrete-time framework. Quantitative results are reported in Fig. 5. While DDPM achieves competitive results on certain categories (e.g., *carpet*, *tile*), it requires 1000 iterative steps, making it over 20× slower than AIAS in practice. DDIM and PLMS, though more efficient, exhibit inconsistent performance across categories and often underperform AIAS, particularly on challenging textures such as

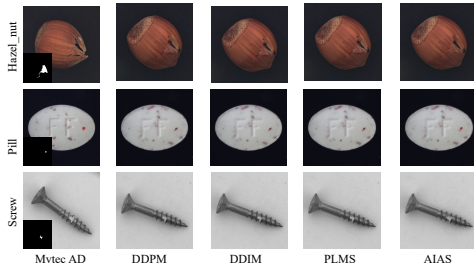


Figure 4: SIAS results with other sampling strategies. **Columns correspond to sampling strategies** (from left to right: ground truth, DDPM (1000 steps), DDIM (50 steps), PLMS (50 steps), AIAS (50 steps), and **rows correspond to categories** (from top to bottom: hazelnut, pill, screw). Further qualitative results (trained on MVTEC and BTAD) are provided in the Supplementary Materials A.8.

capsule, *grid*, and *transistor*. In contrast, AIAS achieves the best results on the majority of categories and consistently provides competitive or superior performance in both mIoU and accuracy, demonstrating its ability to generate segmentation-aligned anomalies with significantly fewer steps. It further indicates that by analytically aggregating multiple DDPM transitions into coarse-to-fine segments, AIAS reduces the discretization error inherent in single-step samplers (e.g., DDIM) or fixed multistep solvers (e.g., PLMS), allowing a closer approximation of the true posterior within just 50 steps. Fig. 4 further illustrates the qualitative advantage. For example, in the *hazel_nut* class, the anomalies produced by DDPM, DDIM, and PLMS display noticeable color inconsistencies near the anomaly boundary, resulting from distributional mismatch with the background. In comparison, FAST-produced anomalies that are well blended into the context, with sharper and more realistic structural alignment.

Table 3: Comparison of pixel-level anomaly segmentation using different steps on the MVTec dataset.

Category	Step 2		Step 5		Step 10		Step 30		Step 50		Step 100		Step 200		Step 500		Step 1000	
	mIoU ↑	Acc ↑	mIoU ↑	Acc ↑	mIoU ↑	Acc ↑	mIoU ↑	Acc ↑	mIoU ↑	Acc ↑	mIoU ↑	Acc ↑	mIoU ↑	Acc ↑	mIoU ↑	Acc ↑	mIoU ↑	Acc ↑
bottle	77.03	80.96	80.55	85.08	83.26	85.90	84.59	87.89	86.86	90.90	83.75	86.95	84.04	88.54	83.52	88.19	81.65	84.83
cable	47.39	48.66	69.58	73.11	71.23	75.07	73.34	77.59	73.71	77.94	72.99	76.50	72.83	76.51	75.23	79.32	73.45	78.06
capsule	43.56	48.58	49.81	54.22	54.85	59.31	61.12	67.08	63.22	71.12	63.15	71.17	62.12	71.76	62.83	70.88	60.01	66.87
carpet	70.24	80.98	73.22	83.18	73.10	84.06	73.56	80.50	73.84	83.53	73.41	82.92	73.17	81.90	73.27	82.49	75.99	84.14
grid	48.15	61.75	50.03	63.28	50.89	71.35	48.76	61.17	52.45	70.70	50.03	65.41	52.06	67.28	49.18	63.63	50.91	63.19
hazel_nut	76.16	78.75	84.16	86.50	90.45	94.04	90.49	94.04	90.81	94.79	90.82	94.16	90.87	94.27	90.77	94.71	89.81	93.31
leather	62.11	66.86	66.74	76.16	67.09	76.51	65.44	72.41	66.60	74.18	66.88	74.22	65.87	87.88	67.95	83.62	71.03	80.32
metal_nut	92.06	93.57	93.94	95.72	94.71	96.98	94.47	96.31	94.65	96.88	94.74	97.19	94.50	96.59	94.72	96.80	94.63	97.18
pill	50.03	55.46	80.01	82.53	90.07	93.80	90.02	94.24	90.17	94.07	89.82	94.10	89.80	93.22	90.15	94.34	89.36	93.79
screw	46.07	52.01	47.92	56.55	50.04	56.21	50.11	60.85	49.94	57.48	50.06	58.66	48.41	61.05	47.71	54.90	49.35	59.18
tile	87.26	93.92	89.46	94.96	89.72	93.92	89.58	93.68	90.13	93.77	89.93	94.45	90.02	93.73	89.71	93.38	91.01	94.72
toothbrush	58.54	67.15	76.65	87.41	76.96	90.29	74.36	90.78	74.98	88.63	74.17	87.29	73.32	86.49	75.66	89.50	76.10	91.25
transistor	66.42	71.59	66.08	70.23	77.27	79.66	89.45	92.65	91.80	94.50	91.39	94.66	89.67	93.50	90.32	93.21	89.59	93.41
wood	68.69	78.28	74.23	81.07	75.97	81.18	78.76	84.99	78.77	86.31	77.00	83.95	77.60	82.85	77.71	83.45	80.03	85.30
zipper	68.85	75.26	70.92	81.44	72.44	84.99	73.08	81.91	72.80	84.73	71.99	81.94	71.71	82.21	71.73	83.47	72.45	82.35
Average	64.17	70.25	71.55	78.10	74.54	81.55	75.81	82.41	76.72	83.97	76.01	82.90	75.73	83.85	76.03	83.46	76.36	83.19

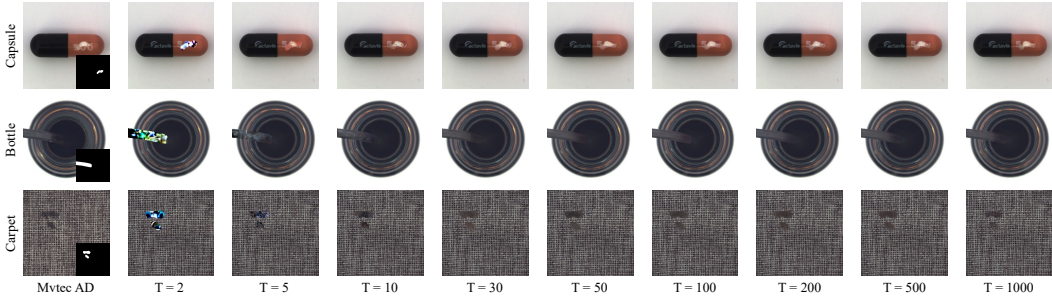


Figure 6: Segmentation-oriented industrial anomaly synthesis results at different steps of AIAS. **Columns correspond to increasing sampling steps T (from left to right), and rows correspond to product categories (from top to bottom: capsule, bottle, carpet).**

The Impact of AIAS under different step sizes. We further investigate the segmentation performance of AIAS under varying numbers of reverse steps, ranging from 2 to 1000, as reported in Table. 3. Remarkably, AIAS approximates the performance of full-step DDPM using only 10 steps, and reaches near-optimal results by 50 steps, demonstrating the effectiveness of our coarse-to-fine aggregation strategy. Performance improves rapidly as t increases from 2 to 50, since early segments capture the global layout and coarse structure of anomalies, which are most relevant for segmentation. This trend is also visually confirmed in Fig. 6. Beyond this point, performance gains gradually saturate, indicating that additional steps primarily refine high-frequency details with limited impact on segmentation accuracy. Notably, when $t = 1000$, AISA degenerates to the original DDPM sampling process, where each segment $[t_e, t_s]$ corresponds to a single denoising step. The convergence of performance

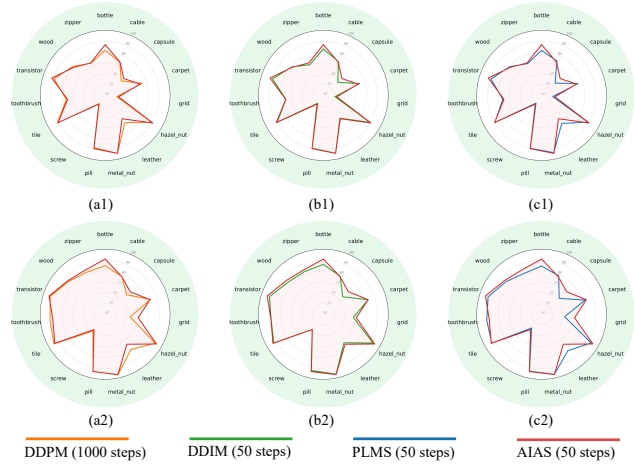


Figure 5: The effect of different sampling methods on SIAS in the MVTec dataset. **Top row** shows per-category segmentation performance using mIoU; **bottom row** shows performance using Acc. **Detailed per-category results of AIAS are reported in Supplementary Material A.6.**

at this point validates that our multi-step analytical updates provide a faithful approximation of the full diffusion trajectory, preserving both global semantics and fine-grained anomaly cues while significantly reducing sampling cost. Furthermore, excessive denoising steps may introduce over-smoothing or amplify reconstruction inconsistencies, potentially weakening the alignment between synthesized anomalies and segmentation-relevant structures. Overall, these results highlight that AIAS not only accelerates sampling, but also introduces an inductive structural bias beneficial for anomaly segmentation. In practice, the optimal balance between quality and efficiency is achieved within 10–50 steps.

The Impact of FARM. To evaluate the effectiveness of FARM, we conduct an ablation study by comparing the model’s performance with (w/ FARM) and without (w/o FARM) FARM under identical AIAS settings. Results on the MVTEc dataset are reported in Fig. 8. The inclusion of FARM leads to substantial improvements in segmentation performance, with average mIoU increasing from 65.33 to 76.42 and accuracy increasing from 71.24 to 83.97. The performance gains are particularly pronounced in challenging categories characterized by fine-grained or complex structures, such as *capsule* ($\uparrow 14.1$ mIoU), *grid* ($\uparrow 14.7$ mIoU), and *transistor* ($\uparrow 29.5$ mIoU). Even in relatively easier categories like *tile* and *hazel_nut*, FARM consistently enhances accuracy and boundary localization, as shown in Fig. 7. **More detailed analysis of FARM can be found in Supplementary Material A.7.**

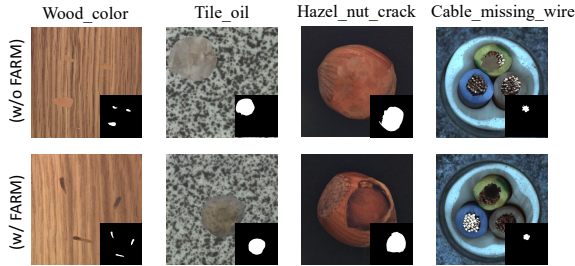


Figure 7: Qualitative ablation results with and without FARM on MVTEc dataset. **Columns correspond to category–anomaly pairs** (from left to right: Wood_color, Tile_oil, Hazel_nut_crack, Cable_missing_wire; and **rows correspond to sampling configurations** (from top to bottom: without FARM (*w/o FARM*) and with FARM (*w/ FARM*)).

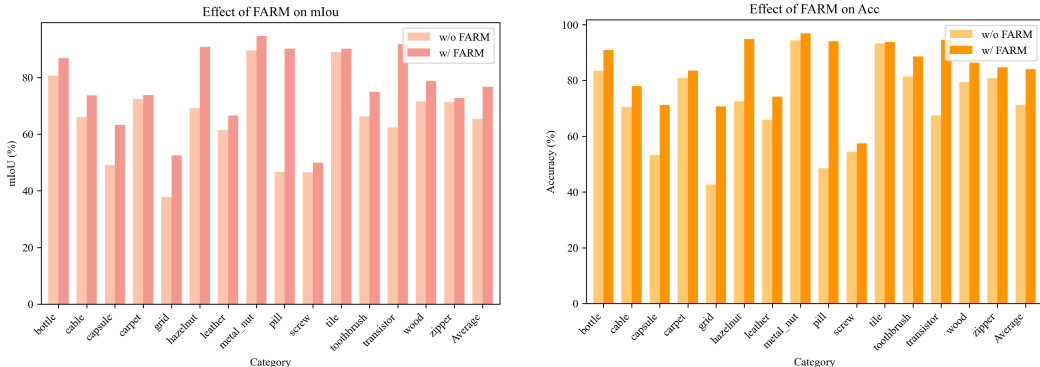


Figure 8: Qualitative ablation results with and without FARM on MVTEc dataset. **Columns correspond to product categories and rows correspond to mIoU and Acc).** **Detailed per-category results for ablation study of FARM are reported in Supplementary Material A.6.**

5 Conclusion

In this work, we proposed **FAST**, a segmentation-oriented foreground-aware diffusion framework tailored for anomaly synthesis. To address the limitations of existing anomaly synthesis methods, specifically their limited controllability and lack of structural awareness, we introduced two key components: the *Foreground-Aware Reconstruction Module* (FARM), which adaptively injects anomaly-aware noise at each sampling step, and the *Anomaly-Informed Efficient Sampling* (AIAS), a training-free strategy that accelerates sampling via coarse-to-fine aggregation. Built upon a discrete-time latent diffusion backbone, FAST enables the synthesis of segmentation-aligned anomalies with as few as 10 denoising steps. Extensive experiments on MVTEc-AD and BTAD demonstrate that FAST outperforms existing baselines in downstream segmentation. FAST represents a promising step toward controllable and efficient segmentation-oriented industrial anomaly synthesis.

References

- [1] Paul Bergmann, Michael Fauser, David Sattlegger, and Carsten Steger. Mvtec ad—a comprehensive real-world dataset for unsupervised anomaly detection. In *Proceedings of the IEEE/CVF conference on computer vision and pattern recognition*, pages 9592–9600, 2019.
- [2] Qiyu Chen, Huiyuan Luo, Chengkan Lv, and Zhengtao Zhang. A unified anomaly synthesis strategy with gradient ascent for industrial anomaly detection and localization. In *European Conference on Computer Vision*, pages 37–54. Springer, 2025.
- [3] M. Cimpoi, S. Maji, I. Kokkinos, S. Mohamed, , and A. Vedaldi. Describing textures in the wild. In *Proceedings of the IEEE Conf. on Computer Vision and Pattern Recognition (CVPR)*, 2014.
- [4] Jacob Devlin, Ming-Wei Chang, Kenton Lee, and Kristina Toutanova. BERT: Pre-training of deep bidirectional transformers for language understanding. In Jill Burstein, Christy Doran, and Tamar Solorio, editors, *Proceedings of the 2019 Conference of the North American Chapter of the Association for Computational Linguistics: Human Language Technologies, Volume 1 (Long and Short Papers)*, pages 4171–4186, Minneapolis, Minnesota, June 2019. Association for Computational Linguistics.
- [5] Zongwei Du, Liang Gao, and Xinyu Li. A new contrastive gan with data augmentation for surface defect recognition under limited data. *IEEE Transactions on Instrumentation and Measurement*, 72:1–13, 2022.
- [6] Yuxuan Duan, Yan Hong, Li Niu, and Liqing Zhang. Few-shot defect image generation via defect-aware feature manipulation. In *Proceedings of the AAAI Conference on Artificial Intelligence*, volume 37, pages 571–578, 2023.
- [7] Yuxuan Duan, Yan Hong, Li Niu, and Liqing Zhang. Few-shot defect image generation via defect-aware feature manipulation. In *Proceedings of the AAAI Conference on Artificial Intelligence*, volume 37, pages 571–578, 2023.
- [8] Mingyuan Fan, Shenqi Lai, Junshi Huang, Xiaoming Wei, Zhenhua Chai, Junfeng Luo, and Xiaolin Wei. Rethinking bisenet for real-time semantic segmentation. In *Proceedings of the IEEE/CVF conference on computer vision and pattern recognition*, pages 9716–9725, 2021.
- [9] Shidan He, Lei Liu, and Shen Zhao. Anomalycontrol: Learning cross-modal semantic features for controllable anomaly synthesis. *arXiv preprint arXiv:2412.06510*, 2024.
- [10] Jonathan Ho, Ajay Jain, and Pieter Abbeel. Denoising diffusion probabilistic models. *Advances in neural information processing systems*, 33:6840–6851, 2020.
- [11] Emiel Hoogeboom and Tim Salimans. Blurring diffusion models. In *The Eleventh International Conference on Learning Representations*, 2023.
- [12] Jie Hu, Yawen Huang, Yilin Lu, Guoyang Xie, Guannan Jiang, Yefeng Zheng, and Zhichao Lu. Anomalyxfusion: Multi-modal anomaly synthesis with diffusion. *arXiv preprint arXiv:2404.19444*, 2024.
- [13] Teng Hu, Jiangning Zhang, Ran Yi, Yuzhen Du, Xu Chen, Liang Liu, Yabiao Wang, and Chengjie Wang. Anomalydiffusion: Few-shot anomaly image generation with diffusion model. In *Proceedings of the AAAI Conference on Artificial Intelligence*, volume 38, pages 8526–8534, 2024.
- [14] Chun-Liang Li, Kihyuk Sohn, Jinsung Yoon, and Tomas Pfister. Cutpaste: Self-supervised learning for anomaly detection and localization. In *Proceedings of the IEEE/CVF conference on computer vision and pattern recognition*, pages 9664–9674, 2021.
- [15] Luping Liu, Yi Ren, Zhijie Lin, and Zhou Zhao. Pseudo numerical methods for diffusion models on manifolds. In *International Conference on Learning Representations*, 2022.
- [16] Cheng Lu, Yuhao Zhou, Fan Bao, Jianfei Chen, Chongxuan Li, and Jun Zhu. Dpm-solver: A fast ode solver for diffusion probabilistic model sampling in around 10 steps. *Advances in Neural Information Processing Systems*, 35:5775–5787, 2022.

- [17] Cheng Lu, Yuhao Zhou, Fan Bao, Jianfei Chen, Chongxuan Li, and Jun Zhu. Dpm-solver++: Fast solver for guided sampling of diffusion probabilistic models. *arXiv preprint arXiv:2211.01095*, 2022.
- [18] Zhaoyang Lyu, Xudong Xu, Ceyuan Yang, Dahua Lin, and Bo Dai. Accelerating diffusion models via early stop of the diffusion process. *arXiv preprint arXiv:2205.12524*, 2022.
- [19] Pankaj Mishra, Riccardo Verk, Daniele Fornasier, Claudio Piciarelli, and Gian Luca Foresti. VT-ADL: A vision transformer network for image anomaly detection and localization. In *30th IEEE/IES International Symposium on Industrial Electronics (ISIE)*, June 2021.
- [20] Shuanlong Niu, Bin Li, Xinggang Wang, and Hui Lin. Defect image sample generation with gan for improving defect recognition. *IEEE Transactions on Automation Science and Engineering*, 17(3):1611–1622, 2020.
- [21] Mingjing Pei, Ningzhong Liu, Bing Zhao, and Han Sun. Self-supervised learning for industrial image anomaly detection by simulating anomalous samples. *International Journal of Computational Intelligence Systems*, 16(1):152, 2023.
- [22] Robin Rombach, Andreas Blattmann, Dominik Lorenz, Patrick Esser, and Björn Ommer. High-resolution image synthesis with latent diffusion models. In *Proceedings of the IEEE/CVF conference on computer vision and pattern recognition*, pages 10684–10695, 2022.
- [23] Hannah M Schlüter, Jeremy Tan, Benjamin Hou, and Bernhard Kainz. Natural synthetic anomalies for self-supervised anomaly detection and localization. In *European Conference on Computer Vision*, pages 474–489. Springer, 2022.
- [24] Qingfeng Shi, Jing Wei, Fei Shen, and Zhengtao Zhang. Few-shot defect image generation based on consistency modeling. In *European Conference on Computer Vision*, pages 360–376. Springer, 2025.
- [25] Jiaming Song, Chenlin Meng, and Stefano Ermon. Denoising diffusion implicit models. In *International Conference on Learning Representations*, 2021.
- [26] Han Sun, Yunkang Cao, and Olga Fink. Cut: A controllable, universal, and training-free visual anomaly generation framework. *arXiv preprint arXiv:2406.01078*, 2024.
- [27] Daniel Watson, William Chan, Jonathan Ho, and Mohammad Norouzi. Learning fast samplers for diffusion models by differentiating through sample quality. In *International Conference on Learning Representations*, 2022.
- [28] Long Wen, You Wang, and Xinyu Li. A new cycle-consistent adversarial networks with attention mechanism for surface defect classification with small samples. *IEEE Transactions on Industrial Informatics*, 18(12):8988–8998, 2022.
- [29] Zhisheng Xiao, Karsten Kreis, and Arash Vahdat. Tackling the generative learning trilemma with denoising diffusion gans. In *International Conference on Learning Representations*, 2022.
- [30] Enze Xie, Wenhai Wang, Zhiding Yu, Anima Anandkumar, Jose M Alvarez, and Ping Luo. Segformer: Simple and efficient design for semantic segmentation with transformers. *Advances in neural information processing systems*, 34:12077–12090, 2021.
- [31] Xichen Xu, Yanshu Wang, Yawen Huang, Jiaqi Liu, Xiaoning Lei, Guoyang Xie, Guannan Jiang, and Zhichao Lu. A survey on industrial anomalies synthesis. *arXiv preprint arXiv:2502.16412*, 2025.
- [32] Minghui Yang, Peng Wu, and Hui Feng. Memseg: A semi-supervised method for image surface defect detection using differences and commonalities. *Engineering Applications of Artificial Intelligence*, 119:105835, 2023.
- [33] Shuai Yang, Zhifei Chen, Pengguang Chen, Xi Fang, Yixun Liang, Shu Liu, and Yingcong Chen. Defect spectrum: a granular look of large-scale defect datasets with rich semantics. In *European Conference on Computer Vision*, pages 187–203. Springer, 2024.

- [34] Hang Yao, Ming Liu, Zhicun Yin, Zifei Yan, Xiaopeng Hong, and Wangmeng Zuo. Glad: towards better reconstruction with global and local adaptive diffusion models for unsupervised anomaly detection. In *European Conference on Computer Vision*, pages 1–17. Springer, 2024.
- [35] Changqian Yu, Changxin Gao, Jingbo Wang, Gang Yu, Chunhua Shen, and Nong Sang. Bisenet v2: Bilateral network with guided aggregation for real-time semantic segmentation. *International journal of computer vision*, 129:3051–3068, 2021.
- [36] Vitjan Zavrtanik, Matej Kristan, and Danijel Skočaj. Draem-a discriminatively trained reconstruction embedding for surface anomaly detection. In *Proceedings of the IEEE/CVF international conference on computer vision*, pages 8330–8339, 2021.
- [37] Gongjie Zhang, Kaiwen Cui, Tzu-Yi Hung, and Shijian Lu. Defect-gan: High-fidelity defect synthesis for automated defect inspection. In *Proceedings of the IEEE/CVF Winter Conference on Applications of Computer Vision*, pages 2524–2534, 2021.
- [38] Ximiao Zhang, Min Xu, and Xiuzhuang Zhou. Realnet: A feature selection network with realistic synthetic anomaly for anomaly detection. In *Proceedings of the IEEE/CVF Conference on Computer Vision and Pattern Recognition*, pages 16699–16708, 2024.
- [39] Xuan Zhang, Shiyu Li, Xi Li, Ping Huang, Jiulong Shan, and Ting Chen. Destseg: Segmentation guided denoising student-teacher for anomaly detection. In *Proceedings of the IEEE/CVF Conference on Computer Vision and Pattern Recognition*, pages 3914–3923, 2023.
- [40] Huangjie Zheng, Pengcheng He, Weizhu Chen, and Mingyuan Zhou. Truncated diffusion probabilistic models and diffusion-based adversarial auto-encoders. In *The Eleventh International Conference on Learning Representations*, 2023.
- [41] Kaiwen Zheng, Guande He, Jianfei Chen, Fan Bao, and Jun Zhu. Diffusion bridge implicit models. In *The Thirteenth International Conference on Learning Representations*, 2025.

A Supplementary Materials

A.1 Proof of Lemma 1

Lemma 1 [Linear–Gaussian closure] Let $\{x_k\}_{k=0}^K \subset \mathbb{R}^d$ satisfy the recursion

$$x_{k-1} = C_k x_k + d_k + \varepsilon_k, \quad \varepsilon_k \sim \mathcal{N}(0, \Sigma_k), \quad \varepsilon_k \perp \{x_k, \varepsilon_{k+1}, \dots\}, \quad (13)$$

where $C_k \in \mathbb{R}^{d \times d}$, $d_k \in \mathbb{R}^d$, and $\Sigma_k \in \mathbb{R}^{d \times d}$ are deterministic. Then, for every integer m with $1 \leq m \leq k$, x_{k-m} is again an affine–Gaussian function of x_k :

$$x_{k-m} = \underbrace{\left(\prod_{i=0}^{m-1} C_{k-i} \right)}_{=: C_k^{(m)}} x_k + \underbrace{\sum_{i=0}^{m-1} \left(\prod_{j=1}^i C_{k-j} \right) d_{k-i}}_{=: d_k^{(m)}} + \varepsilon_k^{(m)}, \quad (14)$$

where

$$\varepsilon_k^{(m)} \sim \mathcal{N}(0, \Sigma_k^{(m)}), \quad \Sigma_k^{(m)} = \sum_{i=0}^{m-1} \left(\prod_{j=1}^i C_{k-j} \right) \Sigma_{k-i} \left(\prod_{j=1}^i C_{k-j} \right)^\top. \quad (15)$$

Proof. :

Base case ($m = 1$).

- Eq. 14 with $m = 1$ is exactly the recursion Eq. 13.

Induction step.

- Assume Eq. 14 and .15 hold for $m = r$ with $1 \leq r < k$:

$$x_{k-r} = C_k^{(r)} x_k + d_k^{(r)} + \varepsilon_k^{(r)}, \quad \varepsilon_k^{(r)} \sim \mathcal{N}(0, \Sigma_k^{(r)}), \quad \varepsilon_k^{(r)} \perp x_k.$$

- Apply Eq. 13 once more:

$$\begin{aligned} x_{k-(r+1)} &= C_{k-r} x_{k-r} + d_{k-r} + \varepsilon_{k-r} \\ &= C_{k-r} (C_k^{(r)} x_k + d_k^{(r)} + \varepsilon_k^{(r)}) + d_{k-r} + \varepsilon_{k-r} \\ &= \underbrace{C_{k-r} C_k^{(r)}}_{C_k^{(r+1)}} x_k + \underbrace{C_{k-r} d_k^{(r)} + d_{k-r}}_{d_k^{(r+1)}} + \underbrace{C_{k-r} \varepsilon_k^{(r)} + \varepsilon_{k-r}}_{\varepsilon_k^{(r+1)}}. \end{aligned} \quad (16)$$

Since $\varepsilon_k^{(r)}$ and ε_{k-r} are independent zero–mean Gaussians, their linear combination $\varepsilon_k^{(r+1)}$ remains Gaussian with covariance $\Sigma_k^{(r+1)} = C_{k-r} \Sigma_k^{(r)} C_{k-r}^\top + \Sigma_{k-r}$, exactly matching Eq. 15 for $m = r + 1$. Hence the statement holds for all m by induction.

Remark 1. The empty product convention $\prod_{j=1}^0 C_{k-j} = I_d$ is used in Eq. 14.

□

A.2 Proof of Lemma 2

Lemma 2 [Closed-form reverse from $t_s \rightarrow t_e$] Fix indices $0 \leq t_e < t_s \leq T$, and let the single-step coefficients (A_t, B_t, σ_t^2) be defined as in Eq. 13. Then the aggregated reverse kernel over $t_s \rightarrow \dots \rightarrow t_e$ is affine–Gaussian:

$$x_{t_e} = \Pi_{t_e}^{t_s} x_{t_s} + \Sigma_{t_e}^{t_s} \hat{x}_0 + \varepsilon_{t_e}, \quad (17)$$

where

$$\Pi_{t_e}^{t_s} := \prod_{i=t_e+1}^{t_s} B_i, \quad \Sigma_{t_e}^{t_s} := \sum_{i=t_e+1}^{t_s} A_i \prod_{j=i+1}^{t_s} B_j, \quad \varepsilon_{t_e} \sim \mathcal{N} \left(0, \sum_{i=t_e+1}^{t_s} \left(\prod_{j=i+1}^{t_s} B_j \right)^2 \sigma_i^2 \mathbf{I} \right).$$

Proof. Apply Lemma 1 with $C_k = B_k$, $d_k = A_k \hat{x}_0$, $\Sigma_k = \sigma_k^2 \mathbf{I}$, and $m = t_s - t_e$. Equations Eq. 17 coincide with the general expressions Eq. 14–Eq. 15, so the result follows directly. \square

A.3 Loss function

The training objective of FAST consists of two components: the standard denoising loss and the reconstruction loss. The denoising loss encourages accurate noise prediction across all spatial regions, while the reconstruction loss ensures that FARM accurately reconstructs anomaly-only content, and allows the inserted noise to remain compatible with the global sampling dynamics, thereby preserving the stability of the overall generation process.

$$\begin{aligned} \mathcal{L}_{\text{FAST}} = & \lambda_1 \cdot \mathbb{E}_{\mathbf{x}_0, \epsilon, t} \left[\|\epsilon - \epsilon_\theta(\mathbf{x}_t, t)\|_2^2 \right] \\ & + \lambda_2 \cdot \mathbb{E}_{\mathbf{x}_0^{\text{an}}, \mathbf{x}_t, \mathcal{M}} \left[\|F_\phi(\mathbf{x}_t, \mathcal{M}, t) - \mathbf{x}_0^{\text{an}}\|_2^2 \right], \end{aligned} \quad (18)$$

where $\epsilon \sim \mathcal{N}(0, \mathbf{I})$ is the reference noise for the denoising target, the \mathbf{x}_0^{an} is the anomaly-only content with pure background, $\epsilon_\theta(\mathbf{x}_t, t)$ and F_ϕ denote LDM and FARM, respectively. The scalar weights λ_1 and λ_2 balance the contributions of the two losses

A.4 Pseudo-code of AIAS

Algorithm 3 Anomaly-Informed Accelerated Sampling

Input: Mask \mathcal{M} , clean background $\mathbf{x}_{\text{full}}^{\text{bg}}$, clean background latent \mathbf{x}_0^{bg} , prediction $\hat{\mathbf{x}}_0$ from ϵ_θ boundary schedule $\mathcal{B} = \{t_1 < t_2 < \dots < t_K = T\}$ and $t_1 = 2$ in our experiments

Output: Synthesised image \mathbf{x}_{full}

Initialize noisy latent $\mathbf{x}_{t_K} \sim \mathcal{N}(0, \mathbf{I})$

for $k = K$ to 1 **do**

$t_s \leftarrow t_k, \quad t_e \leftarrow t_{k-1}$

Coarse multi-step reverse from $t_s \rightarrow t_e$

Define coefficients $A_t = \frac{\sqrt{\bar{\alpha}_{t-1}}\beta_t}{1-\bar{\alpha}_t}$, $B_t = \frac{\sqrt{\bar{\alpha}_t}(1-\bar{\alpha}_{t-1})}{1-\bar{\alpha}_t}$, and $\sigma_t^2 = \frac{1-\bar{\alpha}_{t-1}}{1-\bar{\alpha}_t}\beta_t$

Compute $\mu \leftarrow (\prod_{i=t_e+1}^{t_s} B_i)\mathbf{x}_{t_s} + (\sum_{i=t_e+1}^{t_s} A_i \prod_{j=i+1}^{t_s} B_j)\hat{\mathbf{x}}_0$

Sample noise $\epsilon \sim \mathcal{N}(0, (\sum_{i=t_e+1}^{t_s} (\prod_{j=i+1}^{t_s} B_j)^2 \sigma_i^2)\mathbf{I})$

$\mathbf{x}_{t_e} \leftarrow \mu + \epsilon$

Forward diffuse background to t_e

$\mathbf{x}_{t_e}^{\text{bg}} \sim \mathcal{N}(\sqrt{\bar{\alpha}_{t_e}}\mathbf{x}_0^{\text{bg}}, (1-\bar{\alpha}_{t_e})\mathbf{I})$

$\mathbf{x}_{t_e}^R \leftarrow \text{FARM}(\mathbf{x}_{t_e})$

$\mathbf{x}_{t_e} \leftarrow \mathcal{M} \odot \mathbf{x}_{t_e}^R + (1-\mathcal{M}) \odot \mathbf{x}_{t_e}^{\text{bg}}$

end for

Fine posterior refinement

for $t = t_1$ **down to** 0 **do**

Predict $\hat{\mathbf{x}}_0 \leftarrow f_\theta(\mathbf{x}_t, t)$

$\mathbf{x}_{t-1} \leftarrow q(\mathbf{x}_{t-1} | \mathbf{x}_t, \hat{\mathbf{x}}_0)$

end for

$\mathbf{x}_{\text{full}} \leftarrow \mathcal{M} \odot \text{Decode}(\mathbf{x}_0) + (1-\mathcal{M}) \odot \mathbf{x}_{\text{full}}^{\text{bg}}$

A.5 Training Configuration

To synthesize abnormal data, we utilize the complete set of normal images, their corresponding masks, and associated textual descriptions for each type of anomaly within every category of products. Notably, the original GLASS framework comprises three branches, a normal-sample branch, a feature-level anomaly synthesis branch guided by gradient ascent, and an image-level branch that overlays external textures. Therefore, its output is unsuitable directly for pixel-level anomaly segmentation and other downstream segmentation models. Accordingly, we revised its synthesis process to align with our segmentation-based evaluation protocol. **We release the modified implementation together with the FAST to ensure fairness.**

- **Model Settings.** We set the total number of diffusion steps during training to $T = 1000$. For sampling, the range from step 2 to 1000 is uniformly divided into 50 steps, followed by a fine-grained adjustment phase over the initial steps $[0, 2]$ to enhance reconstruction fidelity. The model is trained with a batch size of 4 and a learning rate of $1.5e-4$. The text embedding E consists of 8 tokens.
- **Prompt Construction.** For the **MVTec** dataset, prompts are formed by appending the anomaly type to the product category name. For **BTAD**, due to anonymized category labels, we use a generic prompt: “*damaged*”. Textual embeddings follow the protocol of AnomalyDiffusion, where each prompt is tokenized into 8 discrete units and embedded using a pre-trained BERT encoder [4].
- **Hardware and Runtime.** All models are trained on a setup of eight NVIDIA A100 GPUs (40GB each), with training proceeding for roughly 80k iterations.

A.6 Other quantitative experiments

We provide extended evaluation results to complement the findings reported in the main manuscript. We present detailed, category-wise performance metrics on the MVTEC and BTAD benchmarks, employing BiSeNet V2 and STDC as the segmentation backbones. Moreover, we further analyze the influence of different sampling strategies—except our AIAS method—on downstream segmentation performance using Segformer.

All experiments are conducted under identical settings to those used in the main study. The results consistently demonstrate that our proposed FAST framework significantly outperforms existing anomaly synthesis techniques in enhancing segmentation accuracy across diverse categories.

Table 4: Evaluation of pixel-level segmentation accuracy on extended MVTEC data using real-time BiSeNet V2.

Category	CutPaste		DRAEM		GLASS		DFMGAN		RealNet		AnomalyDiffusion		FAST	
	mIoU \uparrow	Acc \uparrow	mIoU \uparrow	Acc \uparrow	mIoU \uparrow	Acc \uparrow								
bottle	71.77	78.57	75.13	79.17	57.81	60.79	64.28	71.31	72.16	75.55	75.28	85.11	78.48	83.18
cable	46.00	57.08	53.88	60.96	16.63	16.65	57.09	63.25	51.22	62.32	60.55	74.96	70.91	75.77
capsule	25.97	37.04	36.82	42.19	19.53	51.89	28.40	31.18	35.97	39.39	26.77	32.87	48.56	54.22
carpet	58.98	72.22	68.42	77.21	64.77	73.93	62.13	67.98	8.98	9.01	58.18	64.69	68.94	77.20
grid	24.68	44.17	42.81	63.34	6.50	6.91	10.17	15.23	10.61	11.47	18.98	24.30	39.15	51.78
hazel_nut	47.93	53.57	74.83	81.35	71.54	75.62	79.78	84.37	60.16	65.93	57.26	70.41	88.08	93.45
leather	31.11	58.36	55.07	61.58	57.98	71.84	31.77	34.82	53.77	63.85	50.02	61.60	67.18	74.23
metal_nut	82.95	87.73	91.58	94.73	83.82	85.42	91.17	93.57	88.38	90.73	85.52	90.20	93.62	95.82
pill	55.62	67.04	45.23	48.99	23.88	24.15	82.40	84.30	72.59	86.32	80.87	87.02	85.12	89.60
screw	4.88	6.63	25.08	35.77	12.32	13.11	38.14	40.36	22.35	23.78	23.23	29.91	33.49	41.12
tile	76.25	85.75	86.17	90.45	77.32	80.28	85.69	90.12	77.16	84.84	79.32	85.63	86.86	92.12
toothbrush	35.69	50.45	57.66	79.15	38.86	51.97	48.83	58.76	32.38	37.88	44.33	69.32	73.04	87.34
transistor	44.48	51.79	59.88	65.96	44.93	53.04	76.52	82.13	61.68	68.59	76.34	89.94	91.10	93.81
wood	35.51	46.00	49.82	62.09	36.41	51.10	51.84	63.70	47.29	61.35	52.06	72.75	68.15	72.69
zipper	51.61	63.09	66.88	75.75	61.99	70.07	60.61	71.11	66.09	77.54	57.86	67.64	66.59	78.16
Average	46.23	57.30	59.28	67.91	44.95	52.45	57.92	63.48	50.72	57.24	56.44	67.09	70.62	77.37

Table 5: Evaluation of pixel-level segmentation accuracy on extended MVTEC data using real-time STDC.

Category	CutPaste		DRAEM		GLASS		DFMGAN		RealNet		AnomalyDiffusion		FAST	
	mIoU \uparrow	Acc \uparrow	mIoU \uparrow	Acc \uparrow	mIoU \uparrow	Acc \uparrow								
bottle	71.37	82.19	73.31	78.23	63.22	69.25	67.66	76.52	69.44	75.68	72.66	84.94	76.82	80.65
cable	42.88	54.74	50.02	58.38	49.38	57.80	57.74	62.86	35.97	38.81	59.43	74.22	54.85	60.26
capsule	21.73	30.72	36.31	41.68	22.91	27.18	25.60	27.96	31.08	34.25	22.90	26.06	49.35	55.29
carpet	50.79	66.68	66.28	76.70	63.18	77.85	58.58	71.83	57.48	68.51	56.16	68.47	64.52	75.02
grid	15.24	25.75	30.29	41.50	19.89	24.72	1.39	1.39	5.37	5.85	16.20	24.63	20.82	25.60
hazel_nut	58.48	65.59	78.75	83.66	68.57	85.83	81.77	84.66	70.16	82.40	61.83	92.42	87.96	93.99
leather	38.12	58.63	44.63	56.84	57.53	73.90	21.29	22.28	36.76	53.88	46.98	59.89	60.38	75.90
metal_nut	81.13	86.63	91.12	94.08	83.97	89.37	90.68	92.73	86.85	91.45	85.81	90.06	93.01	95.32
pill	50.00	60.28	55.47	61.05	44.48	48.11	80.41	82.55	63.96	65.96	78.23	84.35	82.15	86.48
screw	2.80	4.98	16.16	23.05	16.81	19.33	34.93	38.76	17.93	18.76	1.27	2.00	17.82	21.25
tile	69.86	78.18	84.75	91.31	79.86	88.65	85.36	89.72	70.29	77.70	76.96	84.07	86.29	93.89
toothbrush	41.19	52.81	53.72	76.55	37.46	40.91	36.78	38.94	33.85	43.03	35.39	48.93	75.76	87.32
transistor	58.24	68.80	65.57	80.31	62.64	69.32	78.38	87.23	62.57	72.45	71.96	83.28	93.01	96.05
wood	31.75	43.27	55.25	60.82	36.31	45.67	26.36	33.13	37.23	43.37	48.90	62.57	72.27	78.06
zipper	47.51	59.24	61.03	68.53	59.07	69.39	44.42	51.83	60.04	71.52	56.77	66.66	52.03	67.69
Average	45.41	55.90	57.51	66.18	51.02	59.15	52.76	58.81	49.27	56.24	52.76	63.50	65.80	72.85

A.7 More analysis of FARM

These improvements of FARM are not only empirically significant, but also consistent with intuitive understanding. **Without FARM, the segmentation-oriented industrial anomaly synthesis relies**

Table 6: Ablation study of FARM on the MVTec dataset using the real-time Segformer.

Category	mIoU (w/o FARM) ↑	Acc (w/o FARM) ↑	mIoU (w/ FARM) ↑	Acc (w/ FARM) ↑
bottle	80.65	83.46	86.86	90.90
cable	65.99	70.50	73.71	77.94
capsule	49.08	53.25	63.22	71.12
carpet	72.46	80.84	73.84	83.53
grid	37.79	42.61	52.45	70.70
hazelnut	69.20	72.55	90.81	94.79
leather	61.42	65.91	66.60	74.18
metal_nut	89.59	94.31	94.65	96.88
pill	46.73	48.44	90.17	94.07
screw	46.48	54.42	49.94	57.48
tile	88.91	93.28	90.13	93.77
toothbrush	66.29	81.40	74.98	88.63
transistor	62.35	67.46	91.80	94.50
wood	71.55	79.47	78.77	86.31
zipper	71.40	80.76	72.80	84.73
Average	65.33	71.24	76.72	83.97

Table 7: Ablation Study of AIAS with other training-free sampling Methods on MVTec-AD data via Segformer.

Category	DDPM (1000 steps)		DDIM (50 steps)		PLMS (50 steps)		AIAS (50 steps)	
	mIoU ↑	Acc ↑	mIoU ↑	Acc ↑	mIoU ↑	Acc ↑	mIoU ↑	Acc ↑
bottle	81.65	84.83	82.87	86.03	81.49	84.44	86.86	90.90
cable	73.45	78.06	74.21	78.41	74.78	78.91	73.71	77.94
capsule	60.01	66.87	58.02	64.03	56.92	61.90	63.22	71.12
carpet	75.99	84.14	75.33	83.58	75.41	82.39	73.84	83.53
grid	50.91	63.19	50.85	67.91	50.43	61.42	52.45	70.70
hazel_nut	89.81	93.31	89.69	93.03	89.42	92.96	90.81	94.79
leather	71.03	80.32	66.00	72.48	71.85	81.47	66.60	74.18
metal_nut	94.63	97.18	94.50	96.47	93.93	96.69	94.65	96.88
pill	89.36	93.79	89.84	93.03	89.93	93.66	90.17	94.07
screw	49.35	59.18	48.89	57.26	48.78	55.62	49.94	57.48
tile	91.01	94.72	89.23	92.90	89.96	93.25	90.13	93.77
toothbrush	76.10	91.25	74.79	88.48	76.02	91.00	74.98	88.63
transistor	89.59	93.41	89.35	92.37	89.17	91.99	91.80	94.50
wood	80.03	85.30	79.29	84.03	79.61	84.65	78.77	86.31
zipper	72.45	82.35	71.01	83.00	72.06	81.02	72.80	84.73
Average	76.36	83.19	75.59	82.20	75.98	82.09	76.72	83.97

solely on frozen pre-trained weights and weak conditioning from learned textual embeddings. This limits the model’s ability to capture the structural characteristics of industrial anomalies, often leading to visually perturbed but semantically uninformative results. In contrast, FARM explicitly reconstructs anomaly-only content from noisy latents and produce spatially localized, anomaly-aware noise into the sampling process. Additionally, by incorporating both spatial masking and timestep encoding, **FARM guides the model to focus on abnormal regions—information that would otherwise be uniformly treated in the absence of FARM.** Together, these mechanisms improve the structural fidelity, localization precision, and segmentation relevance of synthesized anomalies.

A.8 Other qualitative experiments

We also provide additional qualitative results to supplement the main paper. Specifically, we present synthesized anomalies across multiple categories from MVTec and BTAD, along with comparisons against CutPaste, DRAEM, GLASS, RealNet, DFMGAN, and AnomalyDiffusion. Each figure includes both the generated images and their corresponding segmentation masks.

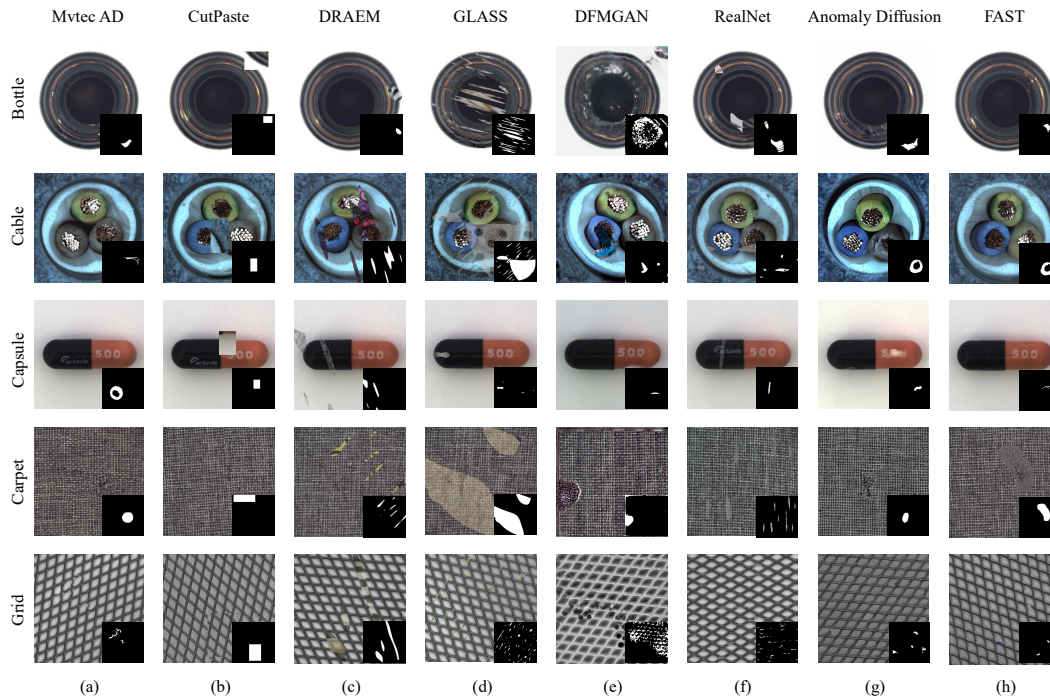


Figure 9: Visualization results of different anomaly synthesis methods on the MVTEc dataset. **Columns correspond to synthesis methods** (from left to right: MVTEc AD, CutPaste, DRAEM, GLASS, DFMGAN, RealNet, Anomaly Diffusion, FAST), and **rows correspond to product categories** (from top to bottom: bottle, cable, capsule, carpet, grid).

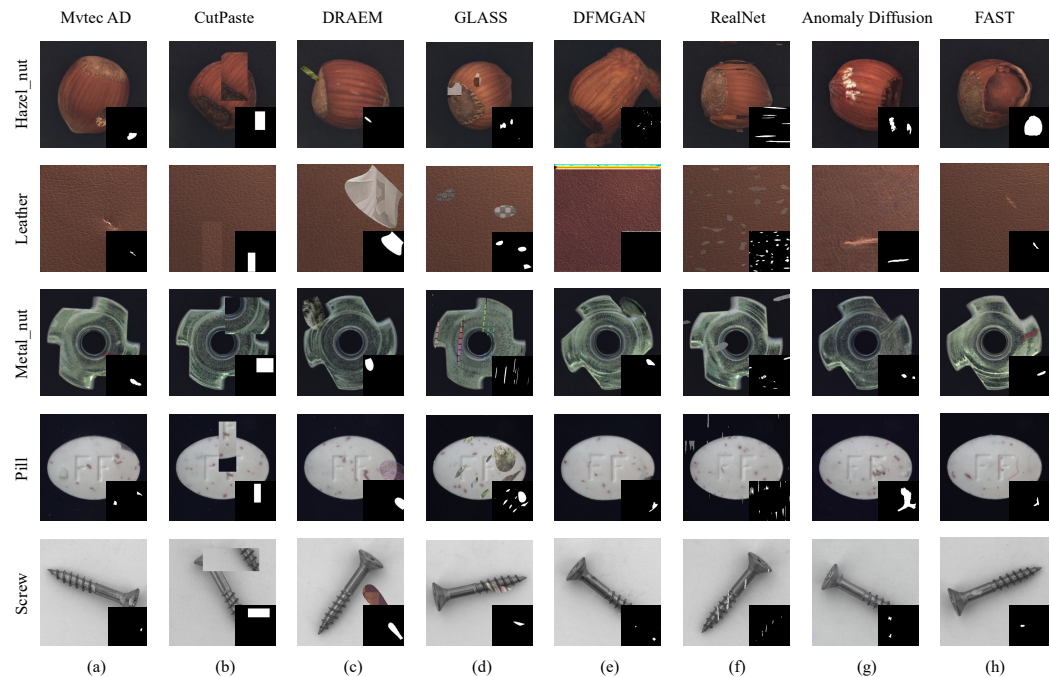


Figure 10: Visualization results of different anomaly synthesis methods on the MVTEc dataset. **Columns correspond to synthesis methods** (from left to right: MVTEc AD, CutPaste, DRAEM, GLASS, DFMGAN, RealNet, Anomaly Diffusion, FAST), and **rows correspond to product categories** (from top to bottom: hazel_nut, leather, metal_nut, pill, screw).

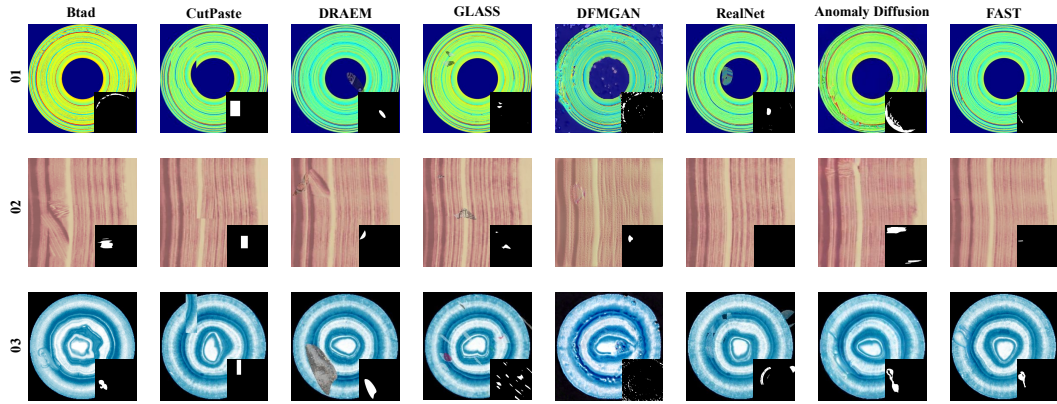


Figure 11: Visualization results of different anomaly synthesis methods on the BTAD dataset. **Columns correspond to synthesis methods** (from left to right: MVTec AD, CutPaste, DRAEM, GLASS, DFMGAN, RealNet, Anomaly Diffusion, FAST), and **rows correspond to product categories**.